Astron. Astrophys. 344, 402–408 (1999)

ASTRONOMY AND ASTROPHYSICS

VLBI polarimetry of the high rotation measure source 3C 119 at 8.4 GHz

R. Nan[1], **D.C. Gabuzda**[2,3], **S. Kameno**[3], **R.T. Schilizzi**[4], **and M. Inoue**[3]

[1] Beijing Astronomical Observatory, A20 Datun Road, Chaoyang District, Beijing 100012, P.R. China
[2] Astro Space Center, Lebedev Physical Institute, 53 Leninsky pr., 117924 Moscow, Russia
[3] National Astronomical Observatory, Osawa 2-21-1, Mitaka, Tokyo 181-8588, Japan
[4] Joint Institute for VLBI in Europe, Postbus 2, 7990 AA, Dwingeloo, The Netherlands

Received 25 November 1998 / Accepted 11 January 1999

Abstract. We have mapped the distribution of the rotation measure of the CSS source 3C 119 on milliarcsecond scales using VLBA observations obtained at three widely-separated frequencies in the available 8.4-GHz band. The resulting images at frequencies 8.16, 8.52, and 8.86 GHz demonstrate that the material associated with the large integrated rotation measure of the source is concentrated near the brightest jet component C. There is a large, smooth gradient of the rotation measure in this component of 2300 rad/m^2/mas, with the largest rotation measure at the leading edge. This supports the idea that C is associated with a collision between the VLBI jet and a dense intergalactic cloud. The magnetic field in C is aligned with the flow into C from the northeast, and swings through $\sim 45^\circ$ so that it remains aligned with the inferred flow toward the emission further down the jet, nearly directly to the south.

Key words: polarization – galaxies: jets – galaxies: magnetic fields – galaxies: quasars: individual: 3C 119 – radio continuum: galaxies

1. Introduction

3C 119 is a typical Compact Steep Spectrum (CSS) radio source with a well defined turnover in its spectrum around 80 MHz and an overall physical extent of ~ 300 pc. It is now generally agreed that CSS sources as a class are small because they are young objects, whose jets have not had time to extend to the larger (kiloparsec) scales usually associated with classical double-lobed radio sources (Fanti et al. 1995, for example); the most recent evidence for this point of view is provided by the proper-motion studies of Owsianik & Conway (1998) and Owsianik et al. (1999). However, it is also likely that at least some CSS sources are small due to the existence of a dense medium that confines the jet to the nuclear region and prevents it from forming larger-scale structure. Using the 45-m telescope at Nobeyama, Kato et al.(1987) and Inoue et al. (1995) measured very large rotation measures for 3C 119 (RM ~ 1700 rad/m^2), and proposed that they were primarily intrinsic to the source; this suggested that 3C 119 might be among those CSS sources whose expansion is hindered by a dense medium.

The earliest Very Long Baseline Interferometry (VLBI) investigations of 3C 119 ($z = 0.408$, V = 20) were made independently at 1.6 GHz with the US VLBI network (Pearson et al. 1980), MERLIN (Spencer et al. 1989), and the European VLBI network (Fanti et al. 1985). The most detailed VLBI studies of the source presented so far have been done at 5 GHz by Fanti et al. (1986) and at 1.6 GHz by Nan et al. (1991). In the latter work, the high dynamic range image reveals a complex spiral-like structure in which a number of components are embedded.

We present below the results of VLBI polarimetry of 3C 119 using the Very Long Baseline Array (VLBA). Simultaneous data were obtained at three significantly different frequencies in the available 8.4-GHz band with nearly identical uv coverage. This has enabled us to determine the polarization properties of the source on milliarcsecond scales, resolve the external Faraday screen in front of the most luminous component, and reveal the geometry and intensity of the intrinsic magnetic fields of the source. This investigation has yielded useful information for our understanding of the energy transport process and interactions between the VLBI jet and its surrounding environment.

2. Observations and data reduction

We obtained 8.4-GHz observations with the VLBA in December 1994 (1994.95). A total of eight baseband converters (BBCs) were used, with four recording right-circular polarization (RCP) and four recording left-circular polarization (LCP). Each BBC had a recording bandwidth of 8 MHz, with 2-bit 16-MHz sampling. In order to study the distribution of the very high rotation measure of 3C 119 on milliarcsecond scales, we spread the different sky frequencies for the four sets of BBCs across the available 8.4-GHz band for the VLBA antennas, which encompasses roughly 840 MHz. By having the individual BBCs observe at widely spaced frequency bands rather than at adjacent frequency bands, we were able to obtain simultaneous polarization images at different frequencies in the 8.4-GHz band, which could then be used to study the rotation measure distribution on milliarcsecond scales.

Send offprint requests to: R. Nan

Table 1. Frequency setup

LO Freq.	BBC Freq.	Sky Freq.	IF
(MHz)	(MHz)	(MHz)	
7604.0	549.49	8153.49–8161.49	1
	557.49	8161.49–8169.49	2
LCP	904.49	8508.49–8516.49	3
USB	912.49	8516.49–8524.49	4
7604.0	549.49	8153.49–8161.49	1
	557.49	8161.49–8169.49	2
RCP	904.49	8508.49–8516.49	3
USB	912.49	8516.49–8524.49	4
9404.0	553.51	8850.49–8858.49	7
	545.51	8858.49–8866.49	8
LCP	895.51	8508.49–8516.49	5
LSB	887.51	8516.49–8524.49	6
9404.0	553.51	8850.49–8858.49	7
	545.51	8858.49–8866.49	8
RCP	895.51	8508.49–8516.49	5
LSB	887.51	8516.49–8524.49	6

Due to technical limitations of the VLBA and BBC distribution system, it was not possible to set the BBCs to observe simultaneously at four arbitrary frequencies in the available band. We overcame this limitation as follows. In order to maximize the total bandwidth over which the BBC frequencies were distributed, to make our rotation measure determinations as reliable as possible, we switched between two local oscillators, obtaining pairs of scans for each "observation" of each source. Each source was observed first using a local oscillator at 7604 MHz (upper side band; LO1), then using a local oscillator at 9404 MHz (lower side band; LO2). The time allowed between scans for the LO switching and general system checks was three minutes. Technical details of our setup, including the local osillator frequencies, BBC frequencies, and resulting sky frequencies are given in Table 1. After concatenating the datasets obtained using the two LOs, the maximum difference between the individual BBC frequencies was about 700 MHz. The integrated rotation measure of 3C 119 (1728 rad/m^2; Kato et al. 1987) corresponds to a rotation of roughly 20° over this bandwidth.

Note that we obtained data in the frequency range 8508.49–8524.49 MHz during the measurements for both of the LOs, making it possible to calibrate the right–left phase difference between LO1 and LO2. There are two pairs of adjacent sky-frequency bands for each LO in the third column of Table 1: 8153.49–8169.59 MHz and 8508.49–8524.49 MHz for LO1 and 8508.49–8524.49 MHz and 8850.49–8866.49 MHz for LO2. We will refer to these four bands as IF12, IF34, IF56, and IF78, as indicated in the last column of Table 1; IF34 and IF56 cover the same frequency range.

We also had observations with the VLA for four hours during our VLBI experiment, only in the frequency range 8508.49–8516.49. This provided information about the integrated total intensity and polarization of the sources observed. We obsered two sources as VLBI calibrators: the bright unpolarized source 3C84, for use in calibrating the polarization cross talk, and the compact polarized source 0300+470 (Gabuzda et al. 1994), for determining the absolute position angle χ of the polarized emission.

The data were calibrated, imaged, and analyzed using the AIPS package. During the entire reduction process, the data at each of the four separate frequencies were processed independently, bearing in mind possible variation in the instrumental polarization across the overall bandwidth. The fringe fitting was done in three steps: (1) manual phase calibration using a short time segment on 3C84, due to lack of phase-cal information in the data; (2) global fringe fitting; and (3) calibration of the right–left delay difference using the AIPS procedure CROSSPOL on scans of 3C84 and 3C 119. In the latter case, we assumed that the phase shift across each individual 8-MHz frequency band due to the source rotation measure was negligible.

After the initial calibration of the data, the data for each source were imaged via self-calibration using the usual AIPS techniques. The instrumental polarization parameters ("D-terms") were determined in two ways: (1) using the model of the total intensity structure of 0300+470, using a linear D-term approximation in the task LPCAL, which allows for the presence of polarization structure in the calibrator source; and (2) using the self-calibrated data for 3C84 using an ellipticity–orientation approximation using the task PCAL. The two D-term solutions obtained were similar; both clearly improved the quality of the polarization map of 0300+470, while the linear D-term solution obtained using LPCAL yielded a higher dynamic range. The D-terms were typically of the order of 1% or less, and the largest D-terms were of the order of 2% (for the Hancock and St. Croix antennas) We adopted the LPCAL D-term solution for our calibration of the 3C 119 data.

The final calibration step–determining the absolute polarization position angle–is very important if we wish to accurately map the magnetic fields on milliarcsecond scales. After the data have been calibrated up to this point, there remains an arbitrary offset in the polarization position angles χ, which is the same for all sources. This offset can be determined using data for a source in which a high fraction of the integrated polarization is present on milliarcsecond scales, by comparing the integrated χ with the χ for the sum of the polarized flux density on milliarcsecond scales, assuming they should be equal. We used the compact source 0300+470 for this purpose.

As a check, we derived the integrated polarizations of 0300+470 and 3C 119 in two ways. One way made use of the VLA data obtained during the VLBI experiment. In addition to observing the three VLBI sources, we observed the primary flux-density and polarization position-angle calibrators 3C48, 3C138, and 3C286 with the VLA. The VLA data for these sources were used to determine the absolute polarization position angle calibration for the VLA data in the usual way. After applying this calibration, the integrated χ values measured for 0300+470 and 3C 119 were 11° and 34°, respectively. We also derived the integrated polarization position angles for these two sources using multi-channel polarimetric data obtained by Inoue

et al. (1995) using the Nobeyama 45-m telescope. The integrated χ values for 0300+470 and 3C 119 yielded by these observations were 9° and 33°, respectively, in very good agreement with our VLA measurements.

The total polarized flux density of 0300+470 on milliarcsecond scales was calculated from the sum of the Q and U flux densities in the images at each of our four frequencies in the VLBA 8.4-GHz band. In order to remove any offsets between frequencies, we applied appropriate rotations to the uv data of all the sources, so as to align the χ values of 0300+470 at each of the frequencies with respect to the value at IF12. This procedure assumes that the Faraday rotation across the observed bandwidth is negligible, as is reasonable given the low rotation measure of 0300+470 (11 rad/m^2) reported by Rudnick & Jones (1983). We then were able to determine the overall rotation needed to calibrate the VLBI χ values by comparing the VLBI χ for 0300+470 with the integrated values indicated by the VLA and Nobeyama measurements indicated above.

Following vector averaging of the two polarization images at IF34 and IF56, which corresponded to the same frequency, we obtained a data cube for 3C 119 at our three observing frequencies. We were then able to map the rotation measures using the AIPS task RM, which performs a weighted fit of the position angle to the λ^2 dependence expected for Faraday rotation.

3. Results

3.1. Total intensity image of 3C 119 at 8.4-GHz

The total intensity structure at one of our three frequencies (8.86 GHz) is shown in Fig. 1; this image has an angular resolution of 1.6x1.2 mas. The I images for the other frequency channels were very similar. The three brightest components, marked A, B, and C in Fig. 1, correspond to features in the image of Nan et al. (1991), and are mapped here in more detail than in the earlier 1.6-GHz image. The observations of Nan et al. (1991) indicated that the core is A, the northernmost feature in Fig. 1. In our observations, A is compact, but shows a slight extension towards the other two bright components to the southwest. The middle component B, separated from A in position angle -135°, also shows a compact feature, but has two-sided extensions elongated along the direction joining the core and C, the brightest knot in our image. A small fraction of the flux density of the very resolved southern component D, which was well defined at 5 GHz (Fanti et al. 1986) and 1.6 GHz (Nan et al. 1991), is visible on this map. Other extended, steep-spectrum structures detected at lower frequencies are not visible here. The map accounts for about 62% of the total flux density of 3C 119 indicated by our VLA measurements (2.86 Jy).

We estimated the flux density present in each component by summing the flux density corresponding to the component using the AIPS task IMSTAT. We present these flux density estimates for components A, B, C, and D in Table 2. Note that the observing frequencies for IF34 and IF56 are the same, as pointed out above; we can see that our flux density estimates for these two independent measurements are quite consistent, and suggest that the uncertainty in our flux density estimates for individual components is a few mJy. We calculated approximate spectral indices α ($S_\nu \propto \nu^\alpha$) for components A, B, C, and D by obtaining linear least-squares fits on a log S_ν–log ν plot. We used an average of the two measurements at 8.52 GHz for the flux density value at that frequency. Although our measurements span a relatively small frequency range, they have the advantage of being simultaneous in time and of having the same resolution at each frequency; for this reason, we prefer to consider only our three measurements, rather than to try to add information from previous observations at other frequencies. The resulting spectral indices are given in Table 2. We can see that the spectral index of A is close to zero, while the spectra of components B, C, and D are steep, with spectral indices ~ -1. This confirms that A is the core, while B, C, and D are optically thin jet components.

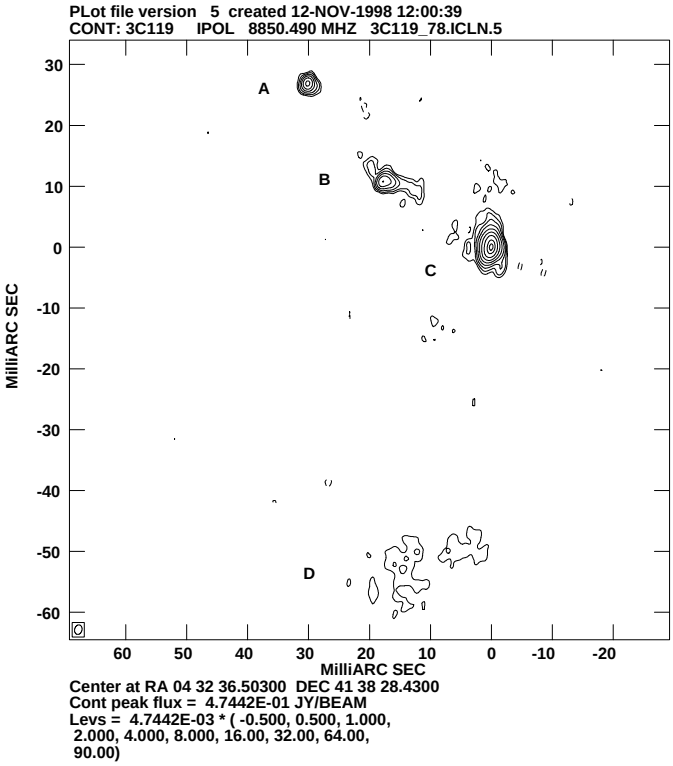

Fig. 1. VLBI total intensity (I) image of 3C 119 at one of our three observing frequencies at epoch 1994.95 (8.86 GHz).

Table 2. Total intensity flux densities for VLBI components in 3C 119

Comp.	IF12	IF34	IF56	IF78	α
A	117	118	117	116	-0.1
B	223	214	219	201	-1.3
C	1440	1409	1416	1311	-1.1
D	27	27	25	24	-1.4

Note: Flux densities are given in mJy/beam; $S_\nu \propto \nu^\alpha$.

3.2. Linear polarization

A contour map of polarized flux density p and a grey-scale I map of 3C 119 at the same frequency as that shown in Fig. 1 are

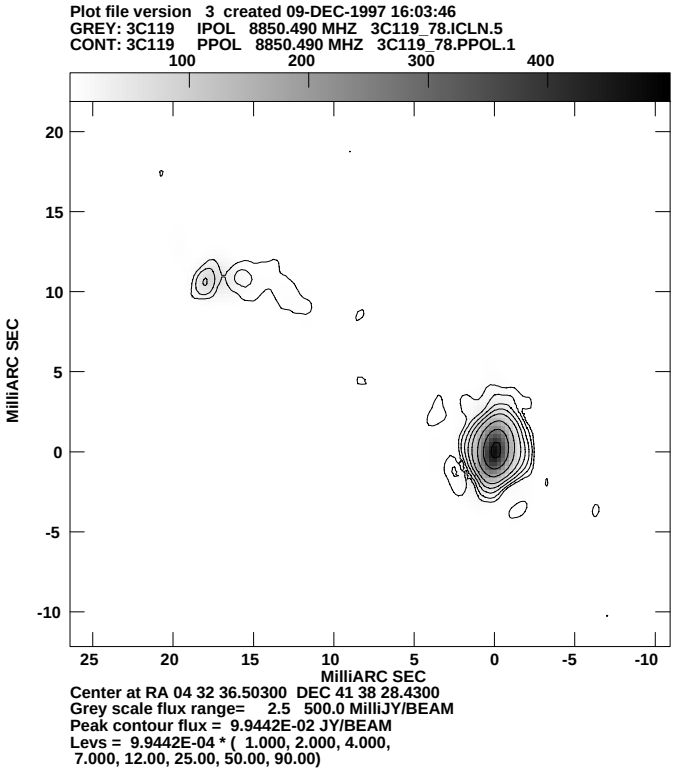

Fig. 2. Superposition of linearly polarized flux density (p) and total intensity (I) images for 3C 119 at one of our three observing frequencies (8.86 GHz).

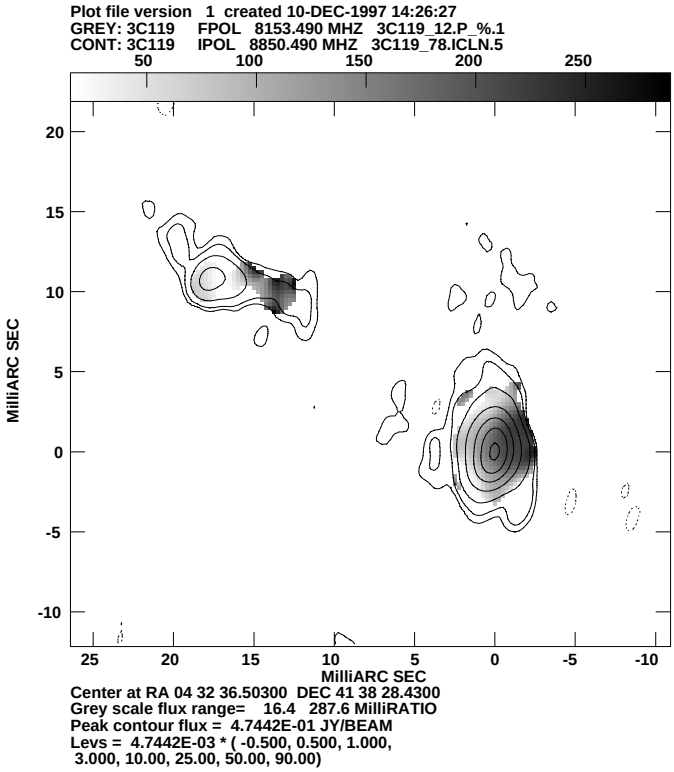

Fig. 3. Superposition of the distribution of the degree of polarization m derived from the two images in Fig. 2 on the total intensity contours shown in Fig. 1 for components B and C.

superimposed in Fig. 2. We detected polarization in components B and C, which are both polarized ~ 15–16%. The polarization structure of component B is knotty and one-sided, and follows the extension of the total intensity elongation toward the west. More than 200 mJy of polarized flux was detected in component C; the peaks of the I and p images are well aligned. Both the I and p distributions of C are quite resolved. Fig. 3 shows a superposition of a contour I image and a grey-scale distribution of the degree of polarization m derived from the superposition of p and I shown in Fig. 2. Although caution must be employed when interpreting m distributions derived in this way, this figure suggests that the leading edges of B and C are more highly polarized than other parts of these features, that the degree of polarization there reaches 25%, and that there is a fairly smooth increase in degree of polarization from east to west across component C. Parameters for components A, B, and C derived from the P maps at the four frequency channels are listed in Table 3. In the case of B and C, the polarization parameters were obtained by summing the Q and U flux densities attributed to those features using the AIPS task IMSTAT. Again, the frequencies measured by IF34 and IF56 are the same; comparison of the p and χ values for these two independent measurements suggests that the uncertainty in p is 2–3 mJy and the uncertainty in χ is about 1°. We have used the level in the P images at which the noise contours become approximately uniform over the map (so that they could hide a weak polarized component) as an upper limit for the polarized flux density of component A; this probably corresponds to approximately a 2-σ limit. The degree of polarization inferred for A in this way is $m < 0.5$–0.7%, showing that the core is quite weakly polarized. It is difficult to place meaningful limits on the polarization of D since it is so heavily resolved; we cannot exclude the possibility that it is fairly highly polarized (up to $\sim 30\%$) if the polarized-flux-density distribution is as diffuse as the I distribution.

Table 3 also shows the vector sum of the polarizations for components B and C measured in each frequency channel. A very interesting point is that the sum of the milliarcsecond-scale polarized flux density for B and C averaged over the three frequencies is 242 mJy in position angle $\chi = 33^\circ$, which is quite close to the integrated polarized flux density for 3C 119 indicated by our VLA data, 238 mJy in $\chi = 34^\circ$; this demonstrates that we have mapped essentially all the integrated polarization in the source at these frequencies, and that only a very small amount of polarized flux is located on more extended scales, beyond our VLBI images.

3.3. Rotation measures and intrinsic magnetic fields

As noted above, the two features for which significant polarization was detected were the two knots B and C. Fig. 4 shows the χ values measured for the total polarization of these two knots at each of the three frequencies we observed, plotted as a function of λ^2. If variations of χ at our different observing frequencies are associated with Faraday rotation, we expect the χ values to

Table 3. Polarization parameters for 3C 119

Comp.	IF12			IF34			IF56			IF78		
	p	χ	m	p	χ	m	p	χ	m	p	χ	m
A	< 0.6	–	< 0.5	< 0.8	–	< 0.7	< 0.6	–	< 0.5	< 0.8	–	< 0.7
B	37	17.9	16.6	36	15.7	16.8	34	16.4	15.5	33	14.9	16.4
C	215	45.2	14.9	226	34.7	16.0	229	36.0	16.2	223	27.0	17.0
total	238	41.6		255	32.2		256	33.6		253	25.5	

Note: p is given in mJy, m in percent, and χ in degrees. We have not listed limits on the polarized flux density of component D, since it is extremely resolved, and any estimates would be very uncertain.

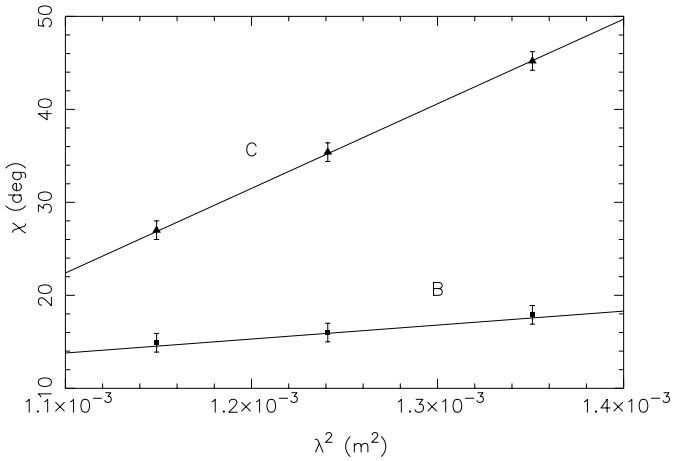

Fig. 4. Plot of the observed χ values for the total polarizations of components C (triangles; upper line) and B (squares; lower line) as a function of λ^2 for the three wavelengths at which we had observations. Errors shown are 1-σ, and are estimated by comparing the χ values for the redundant measurements for 8.52 GHz in Table 3 (IF34 and IF56).

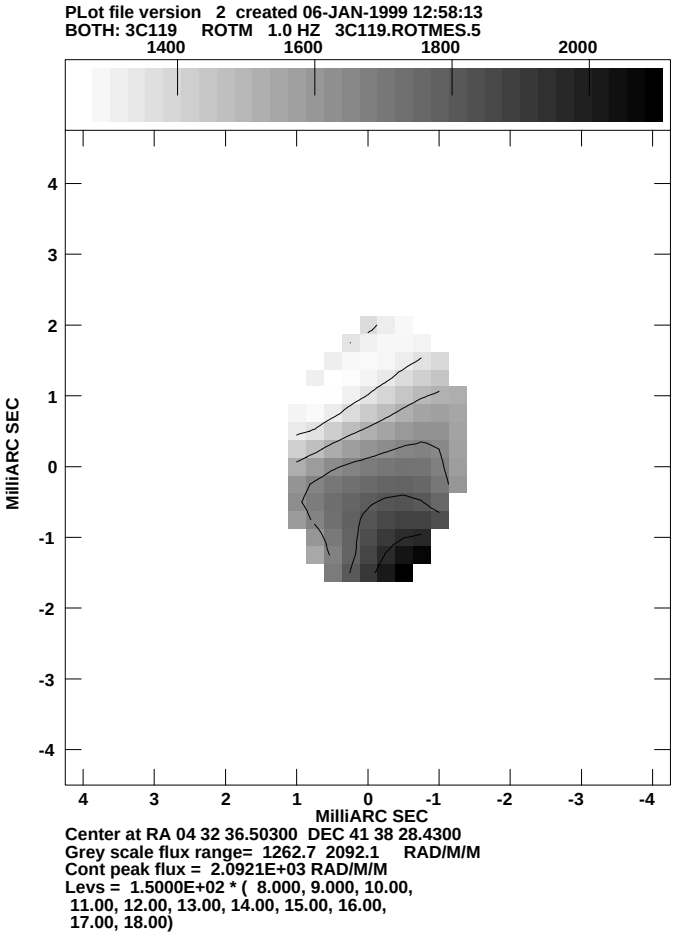

Fig. 5. Rotation-measure distribution in regions where the uncertainty in the local rotation measure is less than ± 500 rad/m^2. We display only the region near component C, since the rotation-measure uncertainties in other regions are larger, and therefore do not appear. A clear gradient in the distribution of the rotation measure across component C is visible.

form a straight line in this plot. We can see that the χ variations for both components B and C can be described well by a λ^2 dependence, indicating the presence of Faraday rotation; the rotation measure of C (about 1590 rad/m^2) is much larger than that of B (about 260 rad/m^2). This demonstrates clearly that material associated with the large integrated rotation measure of 3C 119 is concentrated in the region of component C. If the uncertainty in our χ measurements is roughly $\pm 1^\circ$ (as suggested by a comparison of the χ values for IF34 and IF56 in Table 3), the corresponding uncertainty in the rotation measure is ± 120 rad/m^2. This, again, shows that our estimate for the rotation measure of C, which dominates the polarized flux on milliarcsecond scales, is consistent with the integrated value of 1728 rad/m^2 observed by Kato et al. (1987). No correlations between the local RM and total intensity of the sort found for the high RM source 3C194 (Taylor et al. 1992) are apparent in our images.

The rotation measures were mapped by performing a weighted fit of the position angle to a λ-squared dependence using the AIPS task RM. Fig. 5 shows the magnitude of the rotation measure in the region where the solution errors are below ± 500 rad/m^2, which is equivalent to $\pm 5^\circ$ in χ at each pixel in the map. The area shown is smaller than that in Figs. 2 and 3; the area of low rotation-measure uncertainty in Fig. 5 covers a region about 2.5 x 4 mas in size around component C. The rotation measure distribution smoothly increases from 1200 rad/m^2 in the northeast of component C to 2100 rad/m^2 in the southwest of C, with an average gradient of 2300 rad/m^2 per mas along the direction of elongation of the source structure. This gradient may not be sufficient to cause beam depolarization.

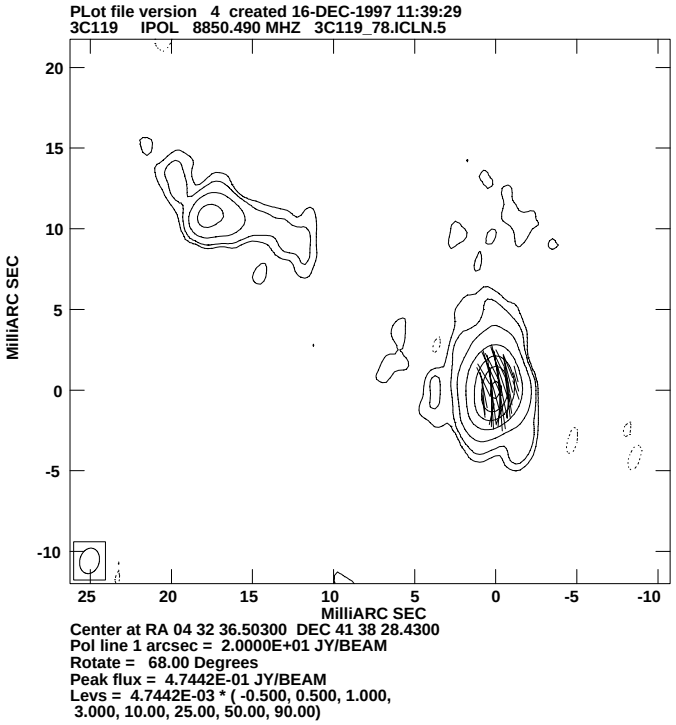

Fig. 6. The same total intensity contours shown in Figs. 1 and 3 for components B and C, with magnetic-field vectors superposed. The intrinsic orientation of the **B** vectors was determined by "derotating" the observed χ vectors using the rotation-measure distribution in Fig. 5.

We can now take into account the rotation measure distribution in 3C 119 to derive the intrinsic direction of the χ vectors for the milliarcsecond-scale polarization. Fig. 6 displays an I contour plot with the intrinsic magnetic field vectors in component C after the output of the task RM (Fig. 5) has been used to "derotate" the observed VLBI χ values. The **B** vectors follow the direction of elongation of the structure, and are roughly perpendicular to the rotation-measure contours in Fig. 5. The **B** field appears to bend toward the south, curving roughly toward the diffuse component D.

4. Discussion

4.1. Faraday rotation measures

There are essentially two possible origins for the high rotation measure of 3C 119: the presence of a dense Galactic cloud along the line of sight to the source, or the presence of thermal plasma near the source, possibly associated with 3C 119 itself. Although typical Galactic rotation measures are tens of rad/m^2, 3C 119 is very close to the Galactic plane (its Galactic latitude is $-4.3°$), making a high Galactic rotation measure more plausible.

If the rotation measure of 3C 119 were Galactic in origin, however, we would expect to see a nearly uniform rotation measure distribution over the source, with any gradients not having any apparent relation to the source structure. Flatters (1998) obtained VLBA observations similar to ours at 5 GHz, which suggested that the rotation measure of 3C 119 was concentrated near component C; however, the resolution and sensitivity provided by those observations were insufficient to draw definitive conclusions about the rotation-measure distribution across C. The $\chi - \lambda^2$ plot in Fig. 4 and 8-GHz rotation-measure distribution in Fig. 5 also demonstrate that the region of high rotation measure is confined to the area near component C; although the uncertainty in the inferred rotation measure for component B is relatively large, it is clear that B's rotation measure is substantially lower than C's. In addition, the resolution provided by our observations has enabled detection of the rotation-measure gradient visible in Fig. 5, which shows a clear relation to the source morphology. This gradient is roughly along the inferred direction of the flow from the place where the western extension of component B joins the northern part of component C to the peak of C.

The rotation-measure gradient across component C is quite large, ~ 2300 rad/m^2 per mas, and increases fairly smoothly from the northeast to southwest, reaching values ~ 2800 rad/m^2 at the southern edge of C. This suggests the presence of a clump of thermal plasma in the intergalactic medium at the leading edge of C. In this case, the rotation-measure gradient in component C in 3C 119 is similar to rotation-measure features associated with the hot spots in Cyg A (Dreher et al. 1987), but on a much smaller scale. In addition, the inference of the presence of a dense cloud at the leading edge of C supports the suggestion by Nan et al. (1991) that the VLBI jet travels from the core to component C, then is deflected at component C and continues south toward component D. In this picture, the brightness of C is associated with compression due to the collision with the dense intergalactic medium.

4.2. Magnetic field

Our observations have, thus, resolved the Faraday screen on milliarcsecond scales. This enables us to "derotate" the observed χ distribution to determine the intrinsic magnetic-field directions at all points in the mas-scale structure where significant polarization was detected. The **B** vectors reconstructed in this way for component C, shown in Fig. 6, are well aligned with the direction of the rotation-measure gradient in Fig. 5. This suggests to us that both the rotation-measure gradient and this **B** field direction reflect the direction of the underlying flow of material in the northern part of component C; i.e., the **B** field there is longitudinal.

Just south of the peak of component C, the **B** field has swung towards the south, toward the direction of component D. It is a quite natural interpretation that this, likewise, reflects the local jet flow direction. As shown in Fig. 3, the degree of polarization in component C is maximum to the west of the peak of C. If, indeed, component C represents the place where the VLBI jet is deflected by a dense clump in the external medium, we would expect the magnetic field to be enhanced by compression. This may provide an explanation for the fact that the maximum degree of polarization in C is located to the west of the I peak: it is displaced toward the region of maximum compression.

4.3. Depolarization

The bandwidth depolarization within each of our 8-GHz frequency channels is estimated to be much less than one percent, so that it is negligible. The relatively high degree of polarization for component C ($\sim 16\%$; see Table 3) and the ordered appearance of the χ distributions for each frequency also suggest that beam depolarization is not important. Together with the fact that our 8-GHz VLBI observations detected a high fraction of the integrated polarization measured by the VLA during our VLBI experiment, this is consistent with the relatively high degree of polarization ($\sim 13\%$) in the 3 cm integrated measurements using the Nobeyama 45-m telescope by Inoue et al. (1995). However, the large rotation-measure gradient in component C will give rise to large differential rotations of the χ vectors associated with the polarized emission in different regions in C at longer wavelengths. This can probably explain the low degree of polarization in integrated measurements at 6 cm ($\sim 1.5\%$).

The degrees of polarization for component C derived from our P maps are 14.9, 16.1 and 17.0%, respectively, at our three different frequency channels, in order of increasing frequency. The two redundant measurements for 8.52 GHz (for IF34 and IF56) differ by only 0.2%, suggesting that this apparent decrease in degree of polarization with decrease in frequency may be real. In contrast, the corresponding three m values for component B are 16.6, 16.2, and 16.4%, so that they do not show any dependence on frequency. If the 2% drop in m across our entire bandwidth for component C is real, this could represent depolarization due to thermal plasma in the emitting region of the synchrotron radiation. This could reflect mixing of the jet material with the thermal plasma of the cloud with which C is colliding.

5. Conclusions

We have presented the results of our analysis of quasi-simultaneous (within $\sim$ 3 minutes) polarization-sensitive VLBA observations of 3C 119 at three separate frequencies within the available 8-GHz band at the VLBA antennas. These observations have allowed us to derive the distribution of the rotation-measure of 3C 119 on parsec scales.

The main features in the VLBI total intensity structure of 3C 119 at 8-GHz are the core A, a weak jet component B in structural position angle -135° from A, the brightest component C further along the jet in this same position angle, and the much more extended component D to the south of these features. The rotation measure in 3C 119 is concentrated around component C, which was tentatively identified by Nan et al. (1991) as the site of a collision between the VLBI jet and a dense external medium. The resolution of our measurements enabled the detection of a large rotation-measure gradient of approximately 2300 rad/m^2/mas across component C. The direction of this gradient coincides with the inferred direction of the flow of jet material into component C. The concentration of the high-rotation-measure region around C and, especially, the observed gradient of the rotation measure in C, which has a clear relation to the source structure, convincingly demonstrates that the thermal plasma giving rise to the large rotation measure of 3C 119 is located near the source, rather than in our Galaxy. The fact that the rotation measure increases toward the leading edge of C provides support for the deflection hypothesis of Nan et al. (1991), in which the VLBI jet is deflected at C toward the southern component D.

The rotation-measure distribution derived can be used to "derotate" the observed χ vectors for the VLBI polarization distribution, enabling a determination of the intrinsic magnetic-field directions on parsec scales. The polarized flux on milliarcsecond scales is dominated by component C. The inferred magnetic field **B** is aligned with the directions of local flows in the region of component C. **B** bends smoothly through roughly 45° from the northeastern to the southwestern edge of component C, from the direction backward toward component B toward the direction forward toward component D. In addition, the rotation-measure gradient is already clearly seen even in the northeast of C, where **B** has not yet begun to rotate, indicating that the rotation-measure gradient is primarily associated with a change in the electron density, rather than with a change in the component of **B** along the line of sight. This behavior is also consistent with the deflection hypothesis of Nan et al. (1991).

Acknowledgements. Rendong Nan is supported by a grant from the National Natural Science Foundation in China. He also acknowledges the hospitality by the NRAO in Socorro, the JIVE institute and NAO during his visits, and thanks Dr. Athol Kemball and Dr. Scott Aaron for their useful suggestions on reduction of these data. We would also like to thank the referee for both prompt and useful comments.

References

Dreher J.W., Carilli C.L., Perley R.A., 1987, ApJ 316, 611
Fanti C., Fanti R., Parma P., Schilizzi R.T., van Breugel W.J.M., 1985, A&A 143, 292
Fanti C., Fanti R., Schilizzi R.T., Spencer R.E., van Breugel W.J.M., 1986, A&A 170, 10
Fanti C., Fanti R., Dallacasa D., et al., 1995, A&A 302, 317
Flatters C., 1998, IAU Colloquium 164: Radio Emission from Galactic and Extragalactic Compact Sources. ASP Conf. Ser. 144, 109
Gabuzda D.C., Mullan C.M., Cawthorne T.V., Wardle J.F.C., Roberts D.H., 1994, AJ 435, 140
Inoue M., Tabara H., Kato T., Aizu K., 1995, PASJ 47, 725
Kato T., Tabara H., Inoue M., Aizu K., 1987, Nat 329, 223
Nan R., Schilizzi R.T., van Breugel W.J.M., et al., 1991, A&A 245, 449
Owsianik I., Conway J.E., 1998, A&A 337, 69
Owsianik I., Conway J.E.,, Polatidis A.G., 1999, New Astronomy Reviews. in press
Taylor G.B., Inoue M., Tabara H., 1992, A&A 264, 415
Pearson T.J., Readhead A.C.S., Wilkinson P.N., 1980, ApJ 236, 714
Rudnick L., Jones T.W., 1983, AJ 88, 518
Spencer R.E., Fanti C., Fanti R., 1989, MNRAS 240, 657